ACS Sustainable Chemistry & Engineering

pubs.acs.org/journal/ascecg

Research Article

Synergistic Effect of Fe Doping and Plasmonic Au Nanoparticles on $W_{18}O_{49}$ Nanorods for Enhancing Photoelectrochemical Nitrogen Reduction

Manh-Hiep Vu,[§] Chinh-Chien Nguyen,[§] and Trong-On Do*

Cite This: *ACS Sustainable Chem. Eng.* 2020, 8, 12321−12330

Read Online

ACCESS | Metrics & More | Article Recommendations | Supporting Information

ABSTRACT: Photoelectrochemical (PEC) nitrogen fixation has opened up new possibilities for the production of ammonia from water and air under mild conditions, but this process is confronted by the inherent challenges associated with theoretical and experimental works, limiting the efficiency of the nitrogen reduction reaction. Herein, we report for the first time a novel and efficient photoelectrocatalytic system, which has been prepared by assembling plasmonic Au nanoparticles with Fe-doped $W_{18}O_{49}$ nanorods (denoted as WOF-Au). (i) The introduction of exotic Fe atoms into nonstoichiometric $W_{18}O_{49}$ can eliminate bulk defects of the $W_{18}O_{49}$ host, which resulted in narrowing bandgap energy and facilitating electron−hole separation and transportation. (ii) Meanwhile, Au nanoparticles combined with a semiconductor induce the localized surface plasmon resonance and generate energetic (hot) electrons, increasing electron density on $W_{18}O_{49}$ nanorods. Consequently, this plasmonic WOF-Au system shows an NH_3 production yield of 9.82 μg h^{-1} cm^{-2} at −0.65 V versus Ag/AgCl, which is ∼2.5-folds higher than that of the WOF (without Au loading), as well as very high stability, and no NH_3 formation was found for the bare $W_{18}O_{49}$ (WO). This high activity can be associated with the synergistic effects between the Fe dopant and plasmonic Au NPs on the host semiconductor $W_{18}O_{49}$. This work can bring some insights into the target-directed design of efficient plasmonic hybrid systems for N_2 fixation and artificial photocatalysis.

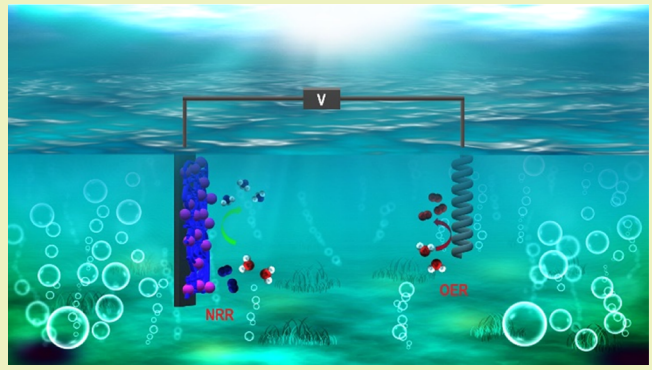

KEYWORDS: *photoelectrocatalytic nitrogen fixation, surface plasmon resonance, tungsten oxide, bulk defects, ammonia synthesis, mild condition*

INTRODUCTION

Natural ammonia (NH_3) synthesis has been considered to be one of the essential processes for the growth and development of living organisms because it plays a crucial role in metabolic pathways.[1] Additionally, it is well known that ammonia can be used as a useful source in manufacturing industries such as a chemical intermediate to produce fertilizers, in hydrogen energy storage, and in food manufacturing among others.[2,3] Currently, ammonia is industrially produced mainly from the traditional Haber−Bosch (HB) process under extreme reaction conditions of 400−450 °C and 200−250 bar.[4,5] For this HB process, ammonia is produced from nitrogen and hydrogen obtained from steam-methane reforming, which annually contributes to 3−5% global consumption of natural gas. Furthermore, fossil fuel energy is also used to drive ammonia synthesis, making this process a major contributor to carbon emissions.[6]

Furthermore, for this HB process, high temperature and high pressure are required. Therefore, the development of green and sustainable alternatives for the fixation of N_2 into NH_3 under ambient conditions has fascinated many researchers in this field. Inspired by the fact that biological nitrogenase can reduce nitrogen through the electron-transfer mechanism,[7] photoelectrochemical (PEC) nitrogen fixation recently has attracted numerous research activities because it takes the advantage of solar energy and electricity to generate electrons, offering an facile route for the synthesis of ammonia at room temperature and pressure.[8−10] Although the PEC nitrogen reduction reaction (NRR) has been studied on various semiconducting materials, so far, the high yield of N_2 to NH_3 is still challenging owing to (i) the incredibly stable N≡N bond with a dissociation energy of 945 kJ mol^{-1} and (ii) the competition

Received: July 1, 2020
Published: July 21, 2020

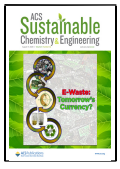

between hydrogen evolution reaction (HER) and NRR.[11] Although both NRR and HER have the same reduction potential, HER only requires two electrons for catalytic reaction, while NRR needs six electrons, making HER more favorable. Various approaches have been introduced to overcome these obstacles, promoting the performance of PEC systems such as loading noble metal cocatalysts and defect engineering (e.g., doping semiconductors with impurity elements or tuning surface lattice vacancies).[12−16]

Recently, Zhang et al. demonstrated that Mo-doped $W_{18}O_{49}$ nanowires could achieve a solar-to-ammonia production rate of 0.195 μmol h^{-1} under simulated AM 1.5 G illumination.[17] On the other hand, Sun et al. indicated that the WO_{3-x} catalysts with tailored surface oxygen vacancies could enhance the yield of NH_3.[18] Although the catalytic activity toward nitrogen reduction of these materials was improved, it is still limited. Tungsten-based oxide (WO_{3-x}) materials have been considered as a promising catalyst for photocatalytic and electrocatalytic NRR; however, these types of materials have never been reported for PEC nitrogen fixation thus far. Even though substoichiometric WO_{3-x} has emerged as a potential candidate for NRR application owing to its high stability, low toxicity, and high redox potential,[19,20] its larger bandgap (2.9 eV) and monoclinic structure containing a limited number of intrinsic oxygen deficiencies[21,22] are the primary bottle-neck restricting the usage of WO_{3-x} for photoelectrochemical NRR. Fe doping can reduce the bandgap energy and improve the visible light absorption ability of semiconductors. Recently, it has been reported that Fe doping can promote the photocatalytic activity of TiO_2 and C_3N_4-based semiconductors for ammonia formation.[23−26]

On the other hand, assembling plasmonic nanoparticles such as gold, silver, aluminum, and copper with a semiconductor can induce the localized surface plasmon resonance (LSPR).[27] Recently, Zhang et al. have successfully prepared a Z-scheme TiO_2/ZnTe/Au nanocorncob.[28] Zhang reported that the LSPR effect of Au nanoparticles can synergistically make effective utilization of broad-range solar light irradiation and enhance the separation efficiency of photogenerated charge carriers. Consequently, the as-prepared sample exhibited high photocatalytic activity toward hydrogen evolution, corresponding to approximately 1%. The intimate contact between noble metal NPs and semiconductors leads to the formation of a Schottky barrier, which inhibits the recombination of photogenerated charge carriers; thus, more active charge carriers are available for the photocatalytic process. The LSPR phenomenon allows the plasmonic metal NPs to concentrate the surrounding light energy and absorb the photons toward the visible light and near IR region to generate energetic (hot) electrons.[29] The hot electrons with high kinetic energy can overcome the Schottky barrier and activate the reactant molecules, consequently enhancing the photocatalytic performance under visible light irradiation.

Inspired by these reasons, in this work, we report a novel photoelectrocatalytic (PEC) system, which is assembled using plasmonic Au nanoparticles with Fe-doped $W_{18}O_{49}$ nanorods (denoted as WOF-Au) for efficient photoelectrocatalytic ammonia production. In this work, (i) Fe doping was used as a medical technique to heal the bulk-defect-states in the nonstoichiometric $W_{18}O_{49}$ lattice as well as enhance visible light absorption and promote the interfacial migration of electrons from the photocatalyst to chemisorbed N_2 molecules. (ii) The decoration of Au nanoparticles on Fe-doped $W_{18}O_{49}$ is to induce the LSPR. This resulting plasmonic WOF-Au system exhibits very high NH_3 production, which is approximately 2.5-folds higher than that of the sample WOF (without Au loading), and high stability. Therefore, this novel photocatalytic system could be a promising technology as a sustainable and alternative method for nitrogen fixation to produce ammonia by photocatalysis.

EXPERIMENTAL SECTION

Materials. Gold(III) chloride trihydrate ($HAuCl_4$), iron(III) chloride anhydrous ($FeCl_3$), tungsten hexachloride (WCl_6), and sodium borohydride ($NaBH_4$) were purchased from Sigma Andric, ethylenediamine and Nafion solution were obtained from Alfa Aesar. Ethanol and distilled water were purchased from commercial sources. All chemical products used in this work were purchased in analytical grade and used without any purification.

Synthesis of Fe-Doped $W_{18}O_{49}$ Nanorods. Fe-doped $W_{18}O_{49}$ nanorods were prepared by the solvothermal method without using any surfactant or capping agent. Briefly, 300 mg of tungsten hexachloride was dissolved into 100 mL of ethanol to obtain a yellow-transparent solution. Afterward, 10 mg of iron(III) chloride was added into the as-prepared solution, which was further vigorously stirred for 30 min. In the next step, the mixture was sealed in a 150 mL Teflon-lined autoclave and heated at 200 °C for 18 h. After cooling down to room temperature, the precipitated product was collected by centrifugation at 9000 rpm for 10 min and washed with anhydrous ethanol three times. Finally, the Fe-doped $W_{18}O_{49}$ sample (WOF) was dried at 70 °C in a vacuum oven overnight for further utilization and characterization. The bare $W_{18}O_{49}$ (WO) nanorods were prepared using the same procedure without adding iron(III) chloride at the initial stage.

Synthesis of Fe-Doped $W_{18}O_{49}$ Nanorods with Au Decoration. 100 mg of the WOF sample was dispersed into 45 mL ethanol and stirred for 1 h for preparing a dark-green solution (solution A). A certain amount of gold(III) chloride trihydrate was dissolved into 1 mL distilled water followed by adding 4 mL of ethylenediamine. Then, the as-prepared gold solution was mixed with solution A and stirred for 2 h. Afterward, 1.97 mg sodium borohydride was added into the mixture, which changed the color of the suspension from dark-green to dark-purple immediately. After 1 h, the suspended product was removed from the mixture and washed with anhydrous ethanol three times. Hence, the obtained product was dried under vacuum overnight to receive Fe-doped $W_{18}O_{49}$ with Au decoration (WOF-Au) powder.

Photocatalyst Characterization. Transmission electron microscopy (TEM) images of the samples were obtained on a JEOL JEM 1230 operated at 120 kV. Powder X-ray diffraction (XRD) patterns of the samples were collected on a Bruker SMART APEXII X-ray diffractometer equipped with a Cu Kα radiation source (λ = 1.5418 Å). X-ray photoelectron spectroscopy (XPS) measurements were carried out in an ion-pumped chamber (evacuated to 10^{-9} Torr) of a photoelectron spectrometer (Kratos Axis-Ultra) equipped with a focused X-ray source (Al Kα, $h\nu$ = 1486.6 eV). The UV−vis absorption spectra were recorded on a Cary 300 Bio UV−vis spectrophotometer. Fourier transform infrared spectra were measured with an FTS 45 infrared spectrophotometer with the KBr pellet technique. The photocurrent measurements were carried out in a conventional three-electrode station (Autolab PGSTAT204).

Photoelectrochemical Measurements. Commercial F-doped SnO_2-coated (FTO) glass was employed as a substrate for loading catalysts. In general, the working electrodes were prepared as follows: 5 mg of the photocatalysts was dispersed in 2 mL anhydrous ethanol to form a slurry of the materials. Then, the slurry was coated onto an FTO glass electrode (1 cm × 1 cm) by the drop-casting method. Next, the as-prepared electrodes were dried naturally overnight under vacuum. Transient photocurrent response was performed using an electrochemical workstation (Autolab PGSTAT204) based on a standard three-electrode system using the as-prepared WOF-Au/FTO cell as the working electrode. A Pt wire and Ag/AgCl cell were used as

https://dx.doi.org/10.1021/acssuschemeng.0c04662
ACS Sustainable Chem. Eng. 2020, 8, 12321−12330

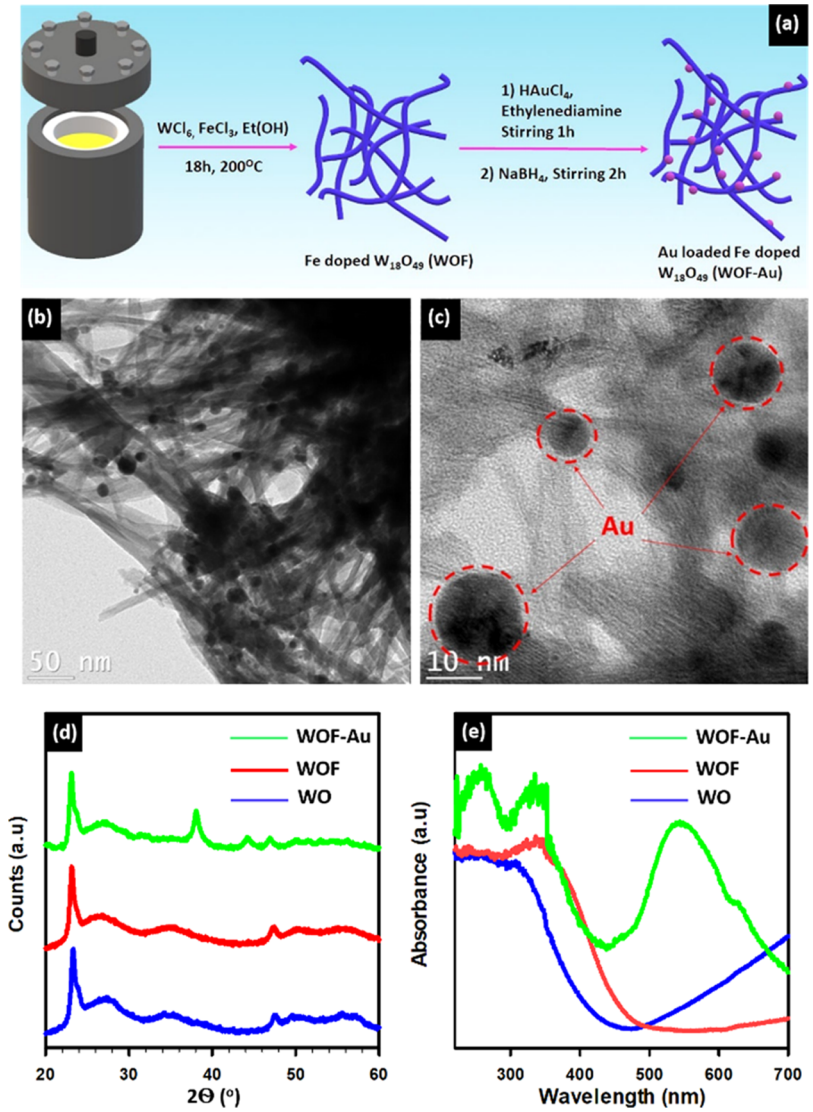

Figure 1. (a) Schematic demonstration of solvothermal synthesis of WOF and WOF-Au nanorods; (b) TEM and (c) HRTEM images of WOF-Au nanorods; (d) XRD spectra of WO, WOF, and WOF-Au samples; (e) UV−vis diffuse reflectance spectra of WOF-Au, WOF, and WO samples.

counter and reference electrodes, respectively. The photocurrent was measured under solar light irradiation (1 sun with AM 1.5 G filter) with 10 s light-on−off cycles with an applied potential of −0.65 V versus Ag/AgCl. For the electrochemical impedance (Nyquist plots) measurements, the perturbation signal was set to be 10 mV, and the frequency range was between 0.1 MHz and 0.1 Hz. The experiment was carried out under solar light illumination. Linear sweep voltammetry (LSV) curves were scanned at a rate of 100 mV/s.

Photoelectrocatalytic Ammonia Production. The as-synthesized catalysts were coated onto carbon papers (WOF-Au/C) as working electrodes. In general, 5 mg of the catalyst was dispersed in 2 mL anhydrous ethanol followed by the addition of 20 μL Nafion solution. Then, the mixture was sonicated for 30 min to form a suspended solution. Afterward, the suspended solution was cast by dropping on carbon paper (1.5 cm × 3.5 cm) and dried under vacuum at 25 °C.

The NRR test was carried out in the self-assembled photoelectrochemical reactor (Figure S1) with an applied potential of −0.65 V versus Ag/AgCl under simulated solar light illumination (1 sun with AM 1.5 G filter) for 2 h. During the test, N_2 gas was continuously bubbled into the electrolyte of 0.5 M Na_2SO_4 (the electrolyte was purged with N_2 for 30 min prior to the test). This procedure was repeated for five cycles, where the electrolyte solution was changed before starting every new cycle. The amount of NH_3 production was determined using the indophenol blue method.

RESULTS AND DISCUSSION

Figure 1a illustrates the synthesis of Fe-doped $W_{18}O_{49}$ with Au decoration via a simple solvothermal method, where ethanol can function as both the morphology-controlling agent and solvent, which provides an appropriate medium for the gradual hydrolysis of WCl_6.[30] Consequently, the slow hydrolysis and shape-controlling agent encourage the growth of rod-like nanostructures. Fe dopants are incorporated into the WOF-Au semiconductor using $FeCl_3$ as the precursor. The presence of the Fe element was proved by energy dispersed X-ray spectroscopy (EDS), as shown in Figure S2. The morphology of the WOF-Au nanorods was confirmed by TEM, featuring two specific dimensions that correspond to the width approximately 10 nm and the length exceeding several hundred nanometers. In the following step, ionic gold chloride adsorbed on the surface of WOF nanorods was reduced to metallic gold nanoparticles in the presence of a sodium borohydride reducing agent. The TEM and high-resolution TEM (HRTEM) images of WOF-Au nanorods are displayed in

https://dx.doi.org/10.1021/acssuschemeng.0c04662
ACS Sustainable Chem. Eng. 2020, 8, 12321−12330

Figure 1b,c, where deposited gold nanoparticles are found to be in a spherical shape with an estimated diameter of 5−10 nm. It can be clearly seen that the Au nanoparticles are highly dispersed on the surface of the nanorods, which have possibly functioned as plasmonic nanoparticles.

Figure 1d shows the XRD patterns of pure (WO) and modified tungsten oxide (WOF and WOF-Au) nanorods, which can be matched well with monoclinic $W_{18}O_{49}$ (JCPDS file 71-2450 as showed in Figure S9). The intense peak located at 23.3° corresponds to the (010) facet, while other diffraction peaks are broadened with low intensities, suggesting that the growth orientation of $W_{18}O_{49}$ nanorods is dominant along the (010) plane.[31] It can be anticipated that the monoclinic skeletal patterns of pure $W_{18}O_{49}$ still remained after doping with the Fe element, without generating a new diffraction peak, which indicates that the incorporation of Fe into $W_{18}O_{49}$ nanorods was successfully formed a homogeneous structure. Otherwise, the XRD patterns of the WOF and WOF-Au samples are observed with slight shifts (≈0.2°) toward the smaller angle compared to the WO sample, suggesting that there was a change in the main crystalline structure during the Fe-doping process. According to Feng and Zhong,[32] this observation is due to the replacement of W by exotic atoms in the lattice structure, leading to the decrement in the number of oxygen defects of $W_{18}O_{49}$ nanorods,[33] which might suggest the reformation of the $W_{18}O_{49}$ lattice from defect states. After decorating with Au nanoparticles, two distinct peaks appeared at 2θ values of 38.1 and 44.3°. These peaks can be ascribed to (111) and (200) reflection planes of the gold cubic phase, respectively, which is in good agreement with the previous report for the standard metallic gold.[34] The highest diffraction intensity at 38.1° implies that the preferential growth orientation of metallic gold was fixed in the (111) direction.

Figure 1e demonstrates the UV−vis absorption spectra of the as-obtained samples at the wavelength ranging between 200 and 700 nm. The WO sample exhibits intense absorption in the UV and near-visible region (<400 nm), which is ascribed to the intrinsic absorption of the $W_{18}O_{49}$ material. Meanwhile, the extended absorption tail of the WO sample could be observed from 500 nm, suggesting incontrovertible evidence for the abundance of surface and bulk phase oxygen defects. Liu et al. and Cong et al. claimed that this extended absorption tail to visible and near-infrared regions apparently implies the high number of oxygen defects and vice versa.[21,35] Although surface oxygen vacancies are particularly beneficial for the separation of charge carriers as well as facilitating the adsorption and dissociation of nitrogen molecules,[36,37] bulk oxygen defects of tungsten suboxide generally act as trapping centers to recombine electrons and holes.[35] According to previous studies, the bulk oxygen defects are unfavorable for the photocatalytic performance of $W_{18}O_{49}$,[38,39] particularly for N_2 fixation. By doping with Fe, the intrinsic absorption edge of the WOF sample is extended up to 500 nm. Moreover, the smooth absorption curve without any observable hump indicates the homogeneous incorporation of Fe into the $W_{18}O_{49}$ lattice structure, which is in accordance with the XRD results. Interestingly, the absorbed intensity of WOF is reduced in the visible region (500−700 nm) as compared to WO, indicating the removal of oxygen defects, which suggests that the structural defects of $W_{18}O_{49}$ were cured by the substitution of W by Fe atoms.[17] After loading Au nanoparticles, the intrinsic absorption profile of the WOF-Au sample was still maintained, except a new peak appearing at around 550 nm. This phenomenon was originated from the LSPR effect on the surface of Au nanoparticles. By using the Kubelka−Munk function, Tauc plots of three samples were plotted using the UV−vis diffuse reflectance spectral data to estimate the optical bandgap energy of the fabricated catalysts (Figure S3). The estimated bandgap of WO is found to be 2.98 eV, while the optical bandgap of WOF and WOF-Au is determined to be a value of 2.65 eV. It can be interpreted that the doping of Fe atoms into the W site creates localized electron-trapping centers, which slightly modified the optical properties of $W_{18}O_{49}$, leading to an extended light absorption in the visible region.

Electron magnetic resonance (EPR) spectra of WO and WOF-Au were further examined to confirm the presence of oxygen vacancies in the samples. As shown in Figure 2, the

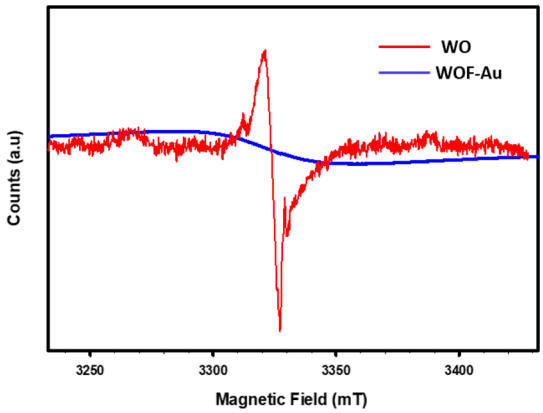

Figure 2. EPR spectra of WO and WOF-Au samples at room temperature.

bulk WO sample exhibited two distinct symmetrical EPR signals at $g \sim 2.002$, which are because of the lone pair electrons on W^{5+} trapped by oxygen vacancies. Whereas, the WOF-Au showed only a weak signal peak. The stronger signal of WO indicates a higher concentration of oxygen vacancies on bulk $W_{18}O_{49}$ in comparison with WOF-Au. This observation suggests that the number of bulk oxygen vacancies was reduced after doping with Fe, which is consistent with the UV−vis results. It can be explained that dopants such as Fe^{3+} can act as electron acceptor centers.[40] When doped with Fe^{3+} impurities, this acceptor-type element can prevent the reduction of W^{6+} to W^{5+} as well as neutralize the donor action of oxygen vacancies, hence, inhibiting the formation of oxygen vacancies.

In order to ascertain the chemical states of the Fe dopant as well as confirming the status of metallic Au, the WOF-Au sample was further analyzed by XPS. As shown in Figure S5, the survey XPS spectrum of WOF-Au indicates the surface of the WOF-Au nanorods is composed of W, Fe, Au, O, and carbon contamination. The high-resolution XPS spectra of W 4f, Fe 2p, Au 4f, and O 1s are obtained and depicted in Figure 3a−d, respectively. As seen in the W 4f spectrum (Figure 3a), the deconvoluted peaks located 35.9 and 38.0 eV could be assigned to W $4f_{7/2}$ and W $4f_{5/2}$ spin−orbit doublets of the W^{6+} oxidation state.[41] In addition to these main peaks, the lower-intensity peaks at 34.3 and 36.5 eV can be ascribed to the +5 oxidation state of W atoms.[42] The weak peaks of W^{5+} species suggest a small number of oxygen vacancies occupying on the surface of WOF-Au nanorods. Similarly, the XPS spectrum of Fe 2p can be fitted into two pairs of peaks, as depicted in

https://dx.doi.org/10.1021/acssuschemeng.0c04662
ACS Sustainable Chem. Eng. 2020, 8, 12321−12330

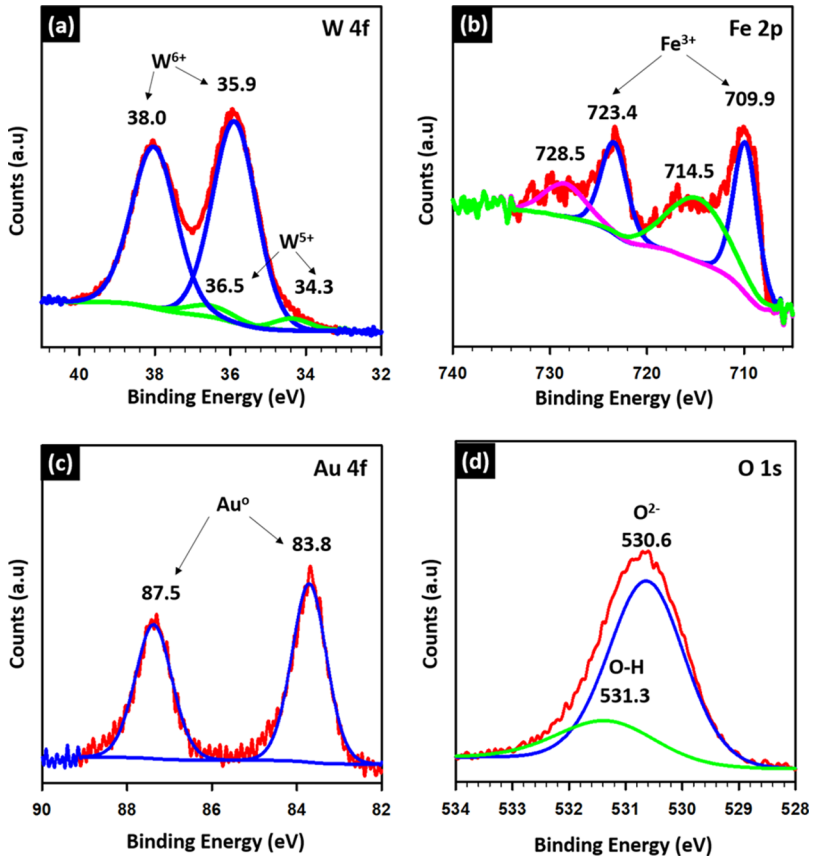

Figure 3. XPS spectra obtained from WOF-Au nanorods: (a) W 4f, (b) Fe 2p, (c) Au 4f, and (d) O 1s spectrum.

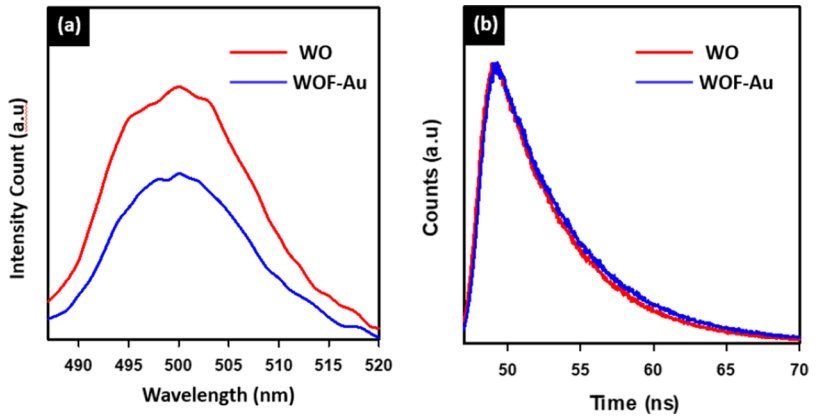

Figure 4. (a) Photoluminescence of the WO and WOF-Au samples; (b) time-resolved photoluminescence of the WO and WOF-Au samples.

Figure 3b. The sharp peaks centered at 709.9 and 723.4 eV correspond to Fe $2p_{3/2}$ and Fe $2p_{1/2}$, respectively. This doublet peak, with a binding energy difference of 13.5 eV, could be the firm evidence for the occurrence of the Fe^{3+} state in the metal−oxide bond,[43] which is in good accordance with the EDS results. Moreover, the satellite peak with a binding energy of 728.5 eV can also be attributed to Fe^{3+} species. Interestingly, another satellite peak is found at 714.5 eV, which is attributed to the binding energy of Fe^{2+} species. The formation of Fe^{2+} species was probably because of the partial reduction of Fe^{3+} along with the presence of neighboring surface oxygen vacancies. These observations are in good agreement with the XPS analysis of W 4f that confirmed the existence of surface oxygen vacancies. The XPS core level spectrum of Au 4f is shown in Figure 3c, where the signals can be separated into two peaks at 83.8 and 87.5 eV. These peaks match with the binding energy of Au $4f_{7/2}$ and Au $4f_{5/2}$, indicating the metallic state[44] of Au nanoparticles on the surface of WOF nanorods, which is consistent with the XRD results. The peak observed at 530.6 eV in the O 1s XPS spectrum is completely associated with the O^{2-} state in the crystal lattice of $W_{18}O_{49}$,[45] while the shoulder peak appearing at 531.3 eV could be originated from the surface-chemisorbed H_2O and OH radicals or other species[46] (Figure 3d).

Figure 4a shows the PL spectra of WO and WOF-Au under an excitation wavelength of 350 nm at room temperature. It is clearly seen that the strong recombination of photogenerated charges in the bulk $W_{18}O_{49}$ sample produced a broad and

https://dx.doi.org/10.1021/acssuschemeng.0c04662
ACS Sustainable Chem. Eng. 2020, 8, 12321−12330

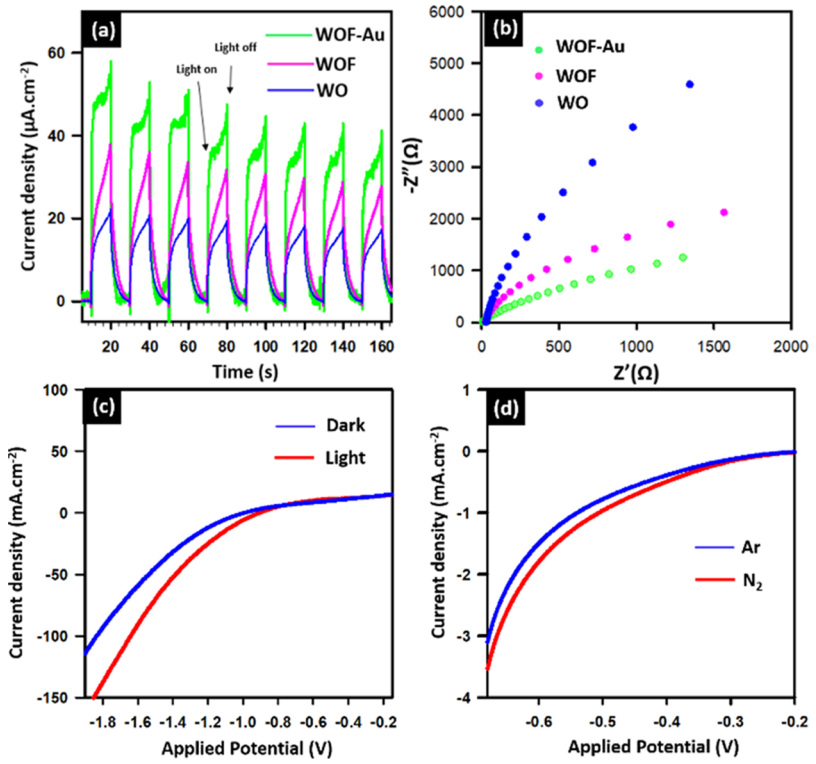

Figure 5. (a) Photocurrent responses of WO, WOF, and WOF-Au at an applied potential of −0.65 V vs Ag/AgCl in 0.5 M Na_2SO_4 under saturated N_2 and (b) Nyquist plots of the samples at an applied potential of −0.65 V vs Ag/AgCl in the 0.5 M Na_2SO_4 electrolyte under saturated N_2 under light irradiation; LSV of the as-prepared WOF-Au sample (c) in the N_2-saturated 0.5 M Na_2SO_4 electrolyte and (d) in N_2- and Ar-saturated 0.5 M Na_2SO_4 electrolytes.

intense peak located at ∼500 nm, which has been reported in many previous works.[47,48] Meanwhile, the steady-state PL spectrum of WOF-Au exhibited a significant PL quenching. Furthermore, WOF-Au also exhibited a longer lifetime of charge carriers than that of WO, as depicted in Figure 4b. The drastically decreased PL intensity and lifetime increase indicate the improvement of charge separation and transportation of the WOF-Au sample, which is originated from the synergistic effect of Fe doping and LSPR of the Au nanoparticles.

In order to gain insight into the charge-transfer efficiency for the fixation of nitrogen, photocurrent measurements of WO, WOF, and WOF-Au were carried out with the repetition of eight on−off cycles under solar light irradiation. The obtained results are illustrated in Figure 5a. The modifications by Fe doping and Au loading show a significant enhancement in current intensity compared to pure $W_{18}O_{49}$, suggesting a noticeable improvement in charge separation and transportation of photogenerated electron−hole. For the initial illumination, the instantaneous photocurrent of WOF-Au can reach 60 μA cm^{-2}. Although the photocurrent decays rapidly and remains stable at a constant current around 45 μA cm^{-2} in the last four cycles, WOF-Au still exhibits a higher current density than WOF and WO samples, which are approximately 28 and 18 μA cm^{-2}, respectively. It is worth noting that the enhancement in photocurrent of WOF-Au is attributed to the incorporation of Fe, which can reduce the number of oxygen vacancies in the bulk structure, minimizing the charge recombination. Moreover, with the LSPR effect, gold nanoparticles can concentrate and absorb higher photon energies, thus, more electrons are generated and transferred to $W_{18}O_{49}$ that significantly promotes the photocurrent density.[49,50]

Furthermore, electrochemical impedance spectroscopy was also engaged to evaluate the charge-transfer resistance (R_{ct}) at the interface of catalyst/electrolyte under light illumination. Theoretically, a small diameter of the Nyquist plot indicates high electronic conductivity as well as low R_{ct}.[51] The Nyquist plot of the WOF electrode exhibits a smaller radius than that of bare $W_{18}O_{49}$, demonstrating a significant improvement of photo-induced charge transportation. The electron-transfer resistance can be further reduced by gold deposition, which is affirmed by the smallest semicircle illustrated in Figure 5b. Hence, the radius following the order of WOF-Au < WOF < WO is consistent with the transient photocurrent of three samples. Otherwise, the Nyquist plot of the WOF-Au electrode in the dark was also recorded and depicted in Figure S6, which exhibits a larger diameter in comparison with the Nyquist semicircle of the WOF-Au electrode under the light irradiation, suggesting a better performance in the exchange current density at the semiconductor/electrolyte interface. This observation can be ascribed to the effect of surface plasmon resonance of metallic gold nanoparticles.[52]

To further understand the performance of the photoelectrocatalytic system, LSV of the WOF-Au/FTO electrode was recorded with and without light irradiation. As expected, a higher current density was observed under the illumination of the solar simulator (Figure 5c). The onset potential of the LSV curve is shifted by 0.15 V versus Ag/AgCl to the more positive potential, suggesting a better catalytic activity for nitrogen fixation than that in the dark. Because the formation of dihydrogen is also one of the primary factors affecting the efficiency of ammonia synthesis,[5] LSV scans of the WOF-Au/C electrode in N_2 and Ar-bubbled environments were also conducted to comprehend the selectivity between HER and

https://dx.doi.org/10.1021/acssuschemeng.0c04662
ACS Sustainable Chem. Eng. 2020, 8, 12321−12330

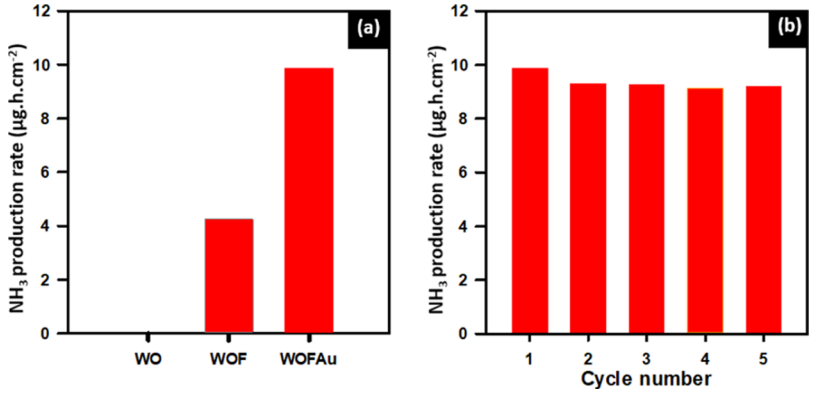

Figure 6. (a) PEC NH_3 production rate of WO, WOF, and WOF-Au samples and (b) recycling test of WOF-Au in N_2-saturated 0.5 M Na_2SO_4 at an applied potential of −0.65 V vs Ag/AgCl.

NRR (Figure 3d). In N_2-saturated 0.5 M Na_2SO_4, a moderate enhancement of current intensity is achieved when the applied voltage sweeps negatively from −0.3 V versus Ag/AgCl, indicating that more photogenerated electrons have been transferred from WOF-Au/C photoelectrochemical cell to absorbed N_2 for producing NH_3. As shown in Figure 5d, the most substantial difference between the two LSV plots is observed at the potential between −0.3 and −0.7 V versus Ag/AgCl. It is presumed that the highest ammonia yield can be obtained at an applied voltage in this potential range. Hence, we have performed the photoelectrocatalytic test of the WOF-Au/C photocathode for nitrogen fixation at an applied potential of −0.65 V versus Ag/AgCl.

The photoelectrochemical N_2 fixation of the as-prepared samples was assessed by their chronoamperometry performance in N_2-saturated 0.5 M Na_2SO_4 over a 2 h-period at room temperature, as shown in Figure 6a. The concentration of ammonia in the electrolyte was determined by the indophenol blue method (see Experimental Section and Figure S7). Under solar light irradiation, WOF and WOF-Au as photocathodes are capable of producing ammonia from nitrogen and water, whereas the WO electrode is inactive for nitrogen reduction. It is worth noting that the significant difference in catalytic performance between bare and doped samples could be attributed to the homogeneous incorporation of Fe dopants. Dopant Fe not only removes bulk structural defects, narrowing the optical bandgap of the semiconductor as well as enabling visible light absorption but also acts as an active site, which captures and accumulates electrons for adsorbed N_2 molecules to dissociate N−N bonding.[23] Under the same conditions, WOF exhibited a production rate of 4.25 $\mu g\ h^{-1}\ cm^{-2}$, which was significantly enhanced to 9.82 $\mu g\ h^{-1}\ cm^{-2}$ after loading with Au nanoparticles. The solar conversion efficiency is calculated to be 0.067%, which is higher than that of previously reported photocatalytic N_2 fixation systems.[53,54] Otherwise, the samples of Au-loaded $W_{18}O_{49}$ (WO-Au) have been prepared and tested. The results showed that $W_{18}O_{49}$-Au exhibited no catalytic activity toward nitrogen reduction, which is similar to the sample of pure $W_{18}O_{49}$. It can be explained that gold nanoparticles only play a role as LSPR and the lack of active sites on WO-Au leads to the inactivity for the conversion of nitrogen to ammonia. Hence, the combination of the Fe dopant for introducing active sites and gold nanoparticles for the LSPR can induce a synergistic effect, which significantly enhances the photoelectrocatalytic performance of the WOF-Au sample. The control experiments were conducted to confirm the source of N_2 for ammonia synthesis. As seen in Figure S8, a trace of ammonia was detected in the Ar-saturated environment. Otherwise, no generation of NH_3 was found when using bare carbon paper as a working electrode or at open-circuit voltage. These observations indicate that NH_3 was primarily evolved from N_2 gas rather than from the other contamination sources. It can also be explained that the detectable amount of ammonia in control experiments was caused by the leakage of atmospheric N_2 absorbed onto the surface of the electrode.[55] Notably, the recyclability of the WOF-Au catalyst was further investigated over five consecutive cycles, as depicted in Figure 6b, which exhibited excellent stability without any noticeable decrement in catalytic activity, suggesting that Fe-doped $W_{18}O_{49}$ with Au decoration could be a promising catalyst for photoelectrochemical nitrogen fixation.

Based on the above experimental results, we proposed a plasmon-induced mechanism for photoelectrocatalytic nitrogen reduction by decorating the Fe-doped $W_{18}O_{49}$ photocathode with Au nanoparticles, as shown in Figure 7. Upon

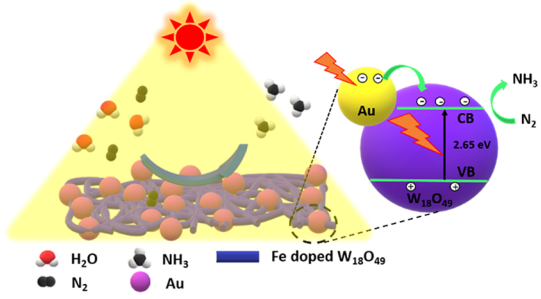

Figure 7. Schematic demonstration of the proposed mechanism for photoelectrochemical nitrogen fixation of the WOF-Au catalyst.

solar light irradiation, electrons are excited to the conduction band (CB) of $W_{18}O_{49}$, leaving highly oxidized holes on the valence band. Because of the abundant structural defects, the photogenerated charge carriers can be rapidly recombined in bulk oxygen vacancies, resulting in poor photoactivity toward the nitrogen reduction of bare WO. However, with the incorporation of Fe impurities, the crystal lattice of $W_{18}O_{49}$ was restored from the bulk-defect-rich state as well as the bandgap energy of WOF was narrowed, which facilitate visible light absorption and promote the separation of photogenerated electron−hole. More importantly, Au nanoparticles on the surface of nanorods take advantage of the LSPR effect to

https://dx.doi.org/10.1021/acssuschemeng.0c04662
ACS Sustainable Chem. Eng. 2020, 8, 12321−12330

generate hot electrons. These energetic electrons facilely traverse the Schottky barrier and inject directly to the CB of the semiconductor. The intrinsic electrons of $W_{18}O_{49}$ and hot electrons then diffuse to the Fe dopants, and further transfer to the absorbed N_2 molecules, facilitating the reduction reaction. Meanwhile, under the driving force of the electric current, generated holes migrate toward the Pt wire electrode for the water oxidation to maintain the charge balance in the photoelectrochemical system.

Apart from the contribution by the above-discussed features, the physical characteristics in the engineered structure such as the small size of Au nanoparticles assembled on the surface of Fe-doped $W_{18}O_{49}$ nanorods enhance the intimate interaction between the cocatalyst and the semiconductor, which could also be considered as the critical factor to determine the efficient photoelectrocatalytic nitrogen reduction of Fe-doped $W_{18}O_{49}$ with Au decoration.

CONCLUSIONS

We demonstrated a new strategy for the synthesis of an efficient plasmonic WOF-Au system, which was obtained through the synthesis of Fe-doped $W_{18}O_{19}$ nanorods followed by in situ deposition of Au nanoparticles. The homogeneous distribution of Fe in $W_{18}O_{49}$ enhances visible light absorption and improves electron−hole separation; while Au nanoparticles decorated in Fe in $W_{18}O_{49}$ induce the LSPR. The resulting plasmonic WOF-Au system has been shown to be very effective for photoelectrochemical nitrogen to ammonia. The high NH_3 production rate (9.82 $\mu g\ h^{-1}\ cm^{-1}$) was obtained under solar light irradiation at −0.65 V versus Ag/AgCl and under ambient conditions, and is ∼2.5-folds higher than that of the Fe-doped $W_{18}O_{19}$ (without Au loading) and much higher than that of bare $W_{18}O_{19}$ with high stability. The high photoelectrocatalytic efficiency of this system could be due to the synergetic effect between Fe dopants and Au nanoparticles in $W_{18}O_{49}$ nanorods.

From the obtained results, it can be concluded that structural engineering and plasmon enhancement could be realized as a promising strategy to develop efficient plasmonic hybrid systems for the photoelectrochemical NRR under solar light. We anticipate that this strategy will be widely adopted as a means of improving photocatalytic performance in a diverse range of photocatalytic reactions.

ASSOCIATED CONTENT

Supporting Information

The Supporting Information is available free of charge at https://pubs.acs.org/doi/10.1021/acssuschemeng.0c04662.

Photoelectrochemical reactor; EDX analysis, Tauc plot, Mott-Schottky plots, XPS survey spectra, electrochemical impedance Nyquist plots, UV−vis spectra, XRD spectra, long-term stability test of the synthesized plasmonic nanorods; and JCPDS data of $W_{18}O_{49}$ (PDF)

AUTHOR INFORMATION

Corresponding Author

Trong-On Do − *Department of Chemical Engineering, Laval University, Quebec, Quebec G1V 0A6, Canada;* orcid.org/0000-0002-7785-5299; Email: trong-on.do@gch.ulaval.ca

Authors

Manh-Hiep Vu − *Department of Chemical Engineering, Laval University, Quebec, Quebec G1V 0A6, Canada*

Chinh-Chien Nguyen − *Department of Chemical Engineering, Laval University, Quebec, Quebec G1V 0A6, Canada; Institute of Research and Development, Duy Tan University, Da Nang 550000, Vietnam*

Complete contact information is available at: https://pubs.acs.org/10.1021/acssuschemeng.0c04662

Author Contributions

[§]M.-H.V. and C.-C.N. contributed equally.

Notes

The authors declare no competing financial interest.

ACKNOWLEDGMENTS

This work was supported by the Natural Science and Engineering Research Council of Canada (NSERC) through the Collaborative Research and Development (CRD), Strategic Project (SP), and Discovery Grants.

REFERENCES

(1) Mendoza, M. L. Z.; Resendis-Antonio, O. Metabolism Nitrogen Fixation. In *Encyclopedia of Systems Biology*; Dubitzky, W., Wolkenhauer, O., Cho, K.-H., Yokota, H., Eds.; Springer New York: New York, NY, 2013; pp 1275−1279

(2) Lan, R.; Tao, S. Ammonia as a Suitable Fuel for Fuel Cells. *Front. Energy Res.* **2014**, *2*, 35.

(3) Klerke, A.; Christensen, C. H.; Nørskov, J. K.; Vegge, T. Ammonia for hydrogen storage: challenges and opportunities. *J. Mater. Chem.* **2008**, *18*, 2304−2310.

(4) Vu, M.-H.; Sakar, M.; Do, T.-O. Insights into the Recent Progress and Advanced Materials for Photocatalytic Nitrogen Fixation for Ammonia (NH_3) Production. *Catalysts* **2018**, *8*, 621.

(5) Vu, M. H.; Sakar, M.; Hassanzadeh-Tabrizi, S. A.; Do, T. O. Photo(electro)catalytic Nitrogen Fixation: Problems and Possibilities. *Adv. Mater. Interfaces* **2019**, *6*, 1900091.

(6) Milton, R. D.; Cai, R.; Abdellaoui, S.; Leech, D.; De Lacey, A. L.; Pita, M.; Minteer, S. D. Bioelectrochemical Haber−Bosch Process: An Ammonia-Producing H_2/N_2 Fuel Cell. *Angew. Chem., Int. Ed.* **2017**, *56*, 2680−2683.

(7) Hoffman, B. M.; Lukoyanov, D.; Yang, Z.-Y.; Dean, D. R.; Seefeldt, L. C. Mechanism of nitrogen fixation by nitrogenase: the next stage. *Chem. Rev.* **2014**, *114*, 4041−4062.

(8) Ye, W.; Arif, M.; Fang, X.; Mushtaq, M. A.; Chen, X.; Yan, D. Efficient Photoelectrochemical Route for the Ambient Reduction of N_2 to NH_3 Based on Nanojunctions Assembled from MoS2 Nanosheets and TiO2. *ACS Appl. Mater. Interfaces* **2019**, *11*, 28809−28817.

(9) Ali, M.; Zhou, F.; Chen, K.; Kotzur, C.; Xiao, C.; Bourgeois, L.; Zhang, X.; MacFarlane, D. R. Nanostructured photoelectrochemical solar cell for nitrogen reduction using plasmon-enhanced black silicon. *Nat. Commun.* **2016**, *7*, 11335.

(10) Zheng, J.; Lyu, Y.; Qiao, M.; Wang, R.; Zhou, Y.; Li, H.; Chen, C.; Li, Y.; Zhou, H.; Jiang, S. P.; Wang, S. Photoelectrochemical Synthesis of Ammonia on the Aerophilic-Hydrophilic Heterostructure with 37.8% Efficiency. *Chem* **2019**, *5*, 617−633.

(11) Medford, A. J.; Hatzell, M. C. Photon-Driven Nitrogen Fixation: Current Progress, Thermodynamic Considerations, and Future Outlook. *ACS Catal.* **2017**, *7*, 2624−2643.

(12) Cheng, M.; Xiao, C.; Xie, Y. Photocatalytic nitrogen fixation: the role of defects in photocatalysts. *J. Mater. Chem. A* **2019**, *7*, 19616−19633.

(13) Feng, X.; Chen, H.; Jiang, F.; Wang, X. Enhanced visible-light photocatalytic nitrogen fixation over semicrystalline graphitic carbon

nitride: Oxygen and sulfur co-doping for crystal and electronic structure modulation. *J. Colloid Interface Sci.* **2018**, *509*, 298−306.
(14) Xue, X.; Chen, R.; Yan, C.; Zhao, P.; Hu, Y.; Zhang, W.; Yang, S.; Jin, Z. Review on photocatalytic and electrocatalytic artificial nitrogen fixation for ammonia synthesis at mild conditions: Advances, challenges and perspectives. *Nano Res.* **2019**, *12*, 1229−1249.
(15) Xue, X.; Chen, R.; Chen, H.; Hu, Y.; Ding, Q.; Liu, Z.; Ma, L.; Zhu, G.; Zhang, W.; Yu, Q.; Liu, J.; Ma, J.; Jin, Z. Oxygen Vacancy Engineering Promoted Photocatalytic Ammonia Synthesis on Ultrathin Two-Dimensional Bismuth Oxybromide Nanosheets. *Nano Lett.* **2018**, *18*, 7372−7377.
(16) Xue, X.; Chen, R.; Yan, C.; Hu, Y.; Zhang, W.; Yang, S.; Ma, L.; Zhu, G.; Jin, Z. Efficient photocatalytic nitrogen fixation under ambient conditions enabled by the heterojunctions of n-type Bi2MoO6 and oxygen-vacancy-rich p-type BiOBr. *Nanoscale* **2019**, *11*, 10439−10445.
(17) Zhang, N.; Jalil, A.; Wu, D.; Chen, S.; Liu, Y.; Gao, C.; Ye, W.; Qi, Z.; Ju, H.; Wang, C.; Wu, X.; Song, L.; Zhu, J.; Xiong, Y. Refining Defect States in $W_{18}O_{49}$ by Mo Doping: A Strategy for Tuning N_2 Activation towards Solar-Driven Nitrogen Fixation. *J. Am. Chem. Soc.* **2018**, *140*, 9434−9443.
(18) Sun, Z.; Huo, R.; Choi, C.; Hong, S.; Wu, T.-S.; Qiu, J.; Yan, C.; Han, Z.; Liu, Y.; Soo, Y.-L.; Jung, Y. Oxygen vacancy enables electrochemical N_2 fixation over WO_3 with tailored structure. *Nano Energy* **2019**, *62*, 869−875.
(19) Tian, H.; Cui, X.; Zeng, L.; Su, L.; Song, Y.; Shi, J. Oxygen vacancy-assisted hydrogen evolution reaction of the Pt/WO3 electrocatalyst. *J. Mater. Chem. A* **2019**, *7*, 6285−6293.
(20) Han, N.; Yang, K. R.; Lu, Z.; Li, Y.; Xu, W.; Gao, T.; Cai, Z.; Zhang, Y.; Batista, V. S.; Liu, W.; Sun, X. Nitrogen-doped tungsten carbide nanoarray as an efficient bifunctional electrocatalyst for water splitting in acid. *Nat. Commun.* **2018**, *9*, 924.
(21) Liu, Q.; Wang, F.; Lin, H.; Xie, Y.; Tong, N.; Lin, J.; Zhang, X.; Zhang, Z.; Wang, X. Surface oxygen vacancy and defect engineering of WO_3 for improved visible light photocatalytic performance. *Catal. Sci. Technol.* **2018**, *8*, 4399−4406.
(22) Li, Y.; Tang, Z.; Zhang, J.; Zhang, Z. Defect Engineering of Air-Treated WO_3 and Its Enhanced Visible-Light-Driven Photocatalytic and Electrochemical Performance. *J. Phys. Chem. C* **2016**, *120*, 9750−9763.
(23) Hu, S.; Chen, X.; Li, Q.; Li, F.; Fan, Z.; Wang, H.; Wang, Y.; Zheng, B.; Wu, G. Fe3+ doping promoted N2 photofixation ability of honeycombed graphitic carbon nitride: The experimental and density functional theory simulation analysis. *Appl. Catal., B* **2017**, *201*, 58−69.
(24) Zhao, W.; Zhang, J.; Zhu, X.; Zhang, M.; Tang, J.; Tan, M.; Wang, Y. Enhanced nitrogen photofixation on Fe-doped TiO_2 with highly exposed (101) facets in the presence of ethanol as scavenger. *Appl. Catal., B* **2014**, *144*, 468−477.
(25) Wei, Z.; Zhang, Y.; Wang, S.; Wang, C.; Ma, J. Fe-doped phosphorene for the nitrogen reduction reaction. *J. Mater. Chem. A* **2018**, *6*, 13790−13796.
(26) Luo, J.; Bai, X.; Li, Q.; Yu, X.; Li, C.; Wang, Z.; Wu, W.; Liang, Y.; Zhao, Z.; Liu, H. Band structure engineering of bioinspired Fe doped $SrMoO_4$ for enhanced photocatalytic nitrogen reduction performance. *Nano Energy* **2019**, *66*, 104187.
(27) Yan, C.; Xue, X.; Zhang, W.; Li, X.; Liu, J.; Yang, S.; Hu, Y.; Chen, R.; Yan, Y.; Zhu, G.; Kang, Z.; Kang, D. J.; Liu, J.; Jin, Z. Well-designed Te/SnS_2/Ag artificial nanoleaves for enabling and enhancing visible-light driven overall splitting of pure water. *Nano Energy* **2017**, *39*, 539−545.
(28) Zhang, W.; Hu, Y.; Yan, C.; Hong, D.; Chen, R.; Xue, X.; Yang, S.; Tian, Y.; Tie, Z.; Jin, Z. Surface plasmon resonance enhanced direct Z-scheme TiO_2/ZnTe/Au nanocorncob heterojunctions for efficient photocatalytic overall water splitting. *Nanoscale* **2019**, *11*, 9053−9060.
(29) Leong, K. H.; Aziz, A. A.; Sim, L. C.; Saravanan, P.; Jang, M.; Bahnemann, D. Mechanistic insights into plasmonic photocatalysts in utilizing visible light. *Beilstein J. Nanotechnol.* **2018**, *9*, 628−648.
(30) Chen, D.; Ge, L.; Yin, L.; Shi, H.; Yang, D.; Yang, J.; Zhang, R.; Shao, G. Solvent-regulated solvothermal synthesis and morphology-dependent gas-sensing performance of low-dimensional tungsten oxide nanocrystals. *Sens. Actuators, B* **2014**, *205*, 391−400.
(31) Sun, S.; Chang, X.; Dong, L.; Zhang, Y.; Li, Z.; Qiu, Y. $W_{18}O_{49}$ nanorods decorated with Ag/AgCl nanoparticles as highly-sensitive gas-sensing material and visible-light-driven photocatalyst. *J. Solid State Chem.* **2011**, *184*, 2190−2195.
(32) Zhong, X.; Sun, Y.; Chen, X.; Zhuang, G.; Li, X.; Wang, J.-G. Mo Doping Induced More Active Sites in Urchin-Like W18O49 Nanostructure with Remarkably Enhanced Performance for Hydrogen Evolution Reaction. *Adv. Funct. Mater.* **2016**, *26*, 5778−5786.
(33) Fang, Z.; Jiao, S.; Kang, Y.; Pang, G.; Feng, S. Photothermal Conversion of $W_{18}O_{49}$ with a Tunable Oxidation State. *ChemistryOpen* **2017**, *6*, 261−265.
(34) Khalil, M. M. H.; Ismail, E. H.; El-Magdoub, F. Biosynthesis of Au nanoparticles using olive leaf extract: 1st Nano Updates. *Arabian J. Chem.* **2012**, *5*, 431−437.
(35) Cong, S.; Yuan, Y.; Chen, Z.; Hou, J.; Yang, M.; Su, Y.; Zhang, Y.; Li, L.; Li, Q.; Geng, F.; Zhao, Z. Noble metal-comparable SERS enhancement from semiconducting metal oxides by making oxygen vacancies. *Nat. Commun.* **2015**, *6*, 7800.
(36) Lv, Y.; Zhu, Y.; Zhu, Y. Enhanced Photocatalytic Performance for the $BiPO_{4-x}$ Nanorod Induced by Surface Oxygen Vacancy. *J. Phys. Chem. C* **2013**, *117*, 18520−18528.
(37) Sadakane, M.; Sasaki, K.; Kunioku, H.; Ohtani, B.; Abe, R.; Ueda, W. Preparation of 3-D ordered macroporous tungsten oxides and nano-crystalline particulate tungsten oxides using a colloidal crystal template method, and their structural characterization and application as photocatalysts under visible light irradiation. *J. Mater. Chem.* **2010**, *20*, 1811−1818.
(38) Shi, L.; Li, Z.; Marcus, K.; Wang, G.; Liang, K.; Niu, W.; Yang, Y. Integration of Au nanoparticles with a g-C3N4 based heterostructure: switching charge transfer from type-II to Z-scheme for enhanced visible light photocatalysis. *Chem. Commun.* **2018**, *54*, 3747−3750.
(39) Hai, G.; Huang, J.; Cao, L.; Jie, Y.; Li, J.; Wang, X. Shape Evolution of Hierarchical $W_{18}O_{49}$ Nanostructures: A Systematic Investigation of the Growth Mechanism, Properties and Morphology-Dependent Photocatalytic Activities. *Nanomaterials* **2016**, *6*, 240.
(40) Steiner, S.; Seo, I. T.; Ren, P.; Li, M.; Keeble, D. J.; Frömling, T. The effect of Fe-acceptor doping on the electrical properties of $Na_{1/2}Bi_{1/2}TiO_3$ and 0.94 $(Na1_{/2}Bi_{1/2})TiO_{3-0.06}$ $BaTiO_3$. *J. Am. Ceram. Soc.* **2019**, *102*, 5295−5304.
(41) Minh Vuong, N.; Kim, D.; Kim, H. Porous Au-embedded WO_3 Nanowire Structure for Efficient Detection of CH4 and H2S. *Sci. Rep.* **2015**, *5*, 11040.
(42) You, L.; Liu, B.; Liu, T.; Fan, B.; Cai, Y.; Guo, L.; Sun, Y. Organic Solar Cells Based on $WO_{2.72}$ Nanowire Anode Buffer Layer with Enhanced Power Conversion Efficiency and Ambient Stability. *ACS Appl. Mater. Interfaces* **2017**, *9*, 12629−12636.
(43) Wang, J.; Zhang, N.; Su, J.; Guo, L. α-Fe_2O_3 quantum dots: low-cost synthesis and photocatalytic oxygen evolution capabilities. *RSC Adv.* **2016**, *6*, 41060−41066.
(44) Martínez, L.; Benito, M.; Mata, I.; Soler, L.; Molins, E.; Llorca, J. Preparation and photocatalytic activity of Au/TiO_2 lyogels for hydrogen production. *Sustainable Energy Fuels* **2018**, *2*, 2284−2295.
(45) Tang, X.; Huang, J.; Liao, H.; Chen, G.; Mo, Z.; Ma, D.; Zhan, R.; Li, Y.; Luo, J. Growth of $W_{18}O_{49}$/WOx/W dendritic nanostructures by one-step thermal evaporation and their high-performance photocatalytic activities in methyl orange degradation. *CrystEngComm* **2019**, *21*, 5905−5914.
(46) McIntyre, N. S.; Zetaruk, D. G. X-ray photoelectron spectroscopic studies of iron oxides. *Anal. Chem.* **1977**, *49*, 1521−1529.
(47) Gong, H.; Cao, Y.; Zhang, Y.; Zhang, Y.; Liu, K.; Cao, H.; Yan, H. The synergetic effect of dual co-catalysts on the photocatalytic activity of square-like WO_3 with different exposed facets. *RSC Adv.* **2017**, *7*, 19019−19025.

https://dx.doi.org/10.1021/acssuschemeng.0c04662
ACS Sustainable Chem. Eng. 2020, 8, 12321−12330

(48) Li, J.; Liu, Y.; Zhu, Z.; Zhang, G.; Zou, T.; Zou, Z.; Zhang, S.; Zeng, D.; Xie, C. A full-sunlight-driven photocatalyst with super long-persistent energy storage ability. *Sci. Rep.* **2013**, *3*, 2409.
(49) Catchpole, K. R.; Polman, A. Design principles for particle plasmon enhanced solar cells. *Appl. Phys. Lett.* **2008**, *93*, 191113.
(50) Clavero, C. Plasmon-induced hot-electron generation at nanoparticle/metal-oxide interfaces for photovoltaic and photocatalytic devices. *Nat. Photonics* **2014**, *8*, 95.
(51) Hou, Y.; Zuo, F.; Dagg, A.; Feng, P. A Three-Dimensional Branched Cobalt-Doped α-Fe_2O_3 Nanorod/$MgFe_2O_4$ Heterojunction Array as a Flexible Photoanode for Efficient Photoelectrochemical Water Oxidation. *Angew. Chem.* **2013**, *125*, 1286−1290.
(52) Nootchanat, S.; Ninsonti, H.; Baba, A.; Ekgasit, S.; Thammacharoen, C.; Shinbo, K.; Kato, K.; Kaneko, F. Investigation of localized surface plasmon/grating-coupled surface plasmon enhanced photocurrent in TiO_2 thin films. *Phys. Chem. Chem. Phys.* **2014**, *16*, 24484−24492.
(53) Shiraishi, Y.; Shiota, S.; Kofuji, Y.; Hashimoto, M.; Chishiro, K.; Hirakawa, H.; Tanaka, S.; Ichikawa, S.; Hirai, T. Nitrogen Fixation with Water on Carbon-Nitride-Based Metal-Free Photocatalysts with 0.1% Solar-to-Ammonia Energy Conversion Efficiency. *ACS Appl. Energy Mater.* **2018**, *1*, 4169−4177.
(54) Hirakawa, H.; Hashimoto, M.; Shiraishi, Y.; Hirai, T. Photocatalytic Conversion of Nitrogen to Ammonia with Water on Surface Oxygen Vacancies of Titanium Dioxide. *J. Am. Chem. Soc.* **2017**, *139*, 10929−10936.
(55) Nazemi, M.; El-Sayed, M. A. Plasmon-enhanced photo-(electro)chemical nitrogen fixation under ambient conditions using visible light responsive hybrid hollow Au-Ag_2O nanocages. *Nano Energy* **2019**, *63*, 103886.

https://dx.doi.org/10.1021/acssuschemeng.0c04662
ACS Sustainable Chem. Eng. 2020, 8, 12321−12330